Electron parameters in the plasma plume of a 5 kW Hall thruster firing with xenon and krypton IEPC

Stéphane Mazouffre, Vincent Delbosq

Electron parameters in the plasma plume of a 5 kW Hall thruster firing with xenon and krypton

IEPC-2024-866

Presented at the 38th International Electric Propulsion Conference, Toulouse, France
June 23-28, 2024

Stéphane Mazouffre*, Vincent Delbosq†

CNRS, ICARE laboratory, 45071 Orléans, France

The PPS®Dual thruster is a 5 kW-class Hall thruster developed by SAFRAN in France. This thruster is able to operate in two distinct modes, namely: a high-curent, i.e. thrust level, mode as well as a high-voltage, i.e. high specific impulse, mode. Such a capacity enables the thruster to respond to a wider variety of space missions and maneuvers. In this contribution we examine the near-field and far-field plasma plume properties of the PPS®Dual thruster in terms of electron parameters. The Hall thruster was fired with both xenon and krypton as propellant for applied voltages from 300 V to 500 V and input power from 3 kW up to 6 kW. Time-resolved Langmuir probe measurements were performed in the vicinity of the channel exit plane as well as far downstream with a probe mounted on a rotating arm in order to explore a large range of angles. Firstly, our analysis shows that the electron energy distribution function departs from the equilibrium distribution, that means a Maxwellian distribution. A Druyvesteyn distribution appears to fit the experimental data better, especially for large electron energies. Secondly, several methods have been used and compared to determine the electron density and the electron temperature. Angular profiles of the electrons parameters are presented for the two gases along with values obtained close to the thruster channel exhaust for many operating conditions. Our study indicates the electron density is larger for xenon while the electron temperature is larger for krypon, as a direct consequence of the ionization energy difference. Moreover, the electron density increases with the propellant mass flow rate and the electron temperature increases with the discharge voltage. Finally, combining density and temperature data, the electron adiabatic exponent was computed. In the far-filed, the value of the exponent is below the value of an atomic gas (5/3) in agreeement with previous works. The exponent is larger for krypton than for xenon. Surprisingly, in the plume far-field the value of the exponent does not depend upon the angular position in spite of large variations in electron density and temperature with the angle. In the plume near-field, no value could be extracted, showing that the exponent is highly dependent on operating conditions.

*Research director, CNRS, ICARE laboratory, stephane.mazouffre@cnrs-orleans.fr
†Research engineer, CNRS, ICARE laboratory vincent.delbosq@cnrs-orleans.fr

Nomenclature

A	Surface area	m^2
d	Diameter	m
e	Elementary charge	C
ε	Kinetic energy	eV
ε_0	Permittivity of free space	F/m
f	Velocity distribution function	m^6/s^3
φ	Latitude	rad
Φ_a	Anode mass flow rate	mg/s
Φ_c	Cathode mass flow rate	mg/s
g	Energy Distribution Function	$m^{-3}\,J^{-1}$
$\hat{g}$	Energy Probability Function	$m^{-3}\,J^{-3/2}$
γ	adiabatic exponent (heat capacity ratio)	-
I_c, I_d	Coil, discharge current	A
I, I_i, I_e	Total, ion, electron current	A
j_i, j_e	Ion, electron current density	A/m^2
k_B	Boltzmann constant	J/K
l	lenght	m
λ_D	Debye length	m
m	Atomic mass	amu
m_e	Electron mass	kg
n_e	Electron density	m^{-3}
p, P	Pressure, Power	Pa, W
r, R	Radius, Thruster–probe distance	m
R_c	Probe circuit resistance	Ω
s, S	Sheath thickness, Slope	m, a.u.
T, T_e	Thrust, Electron temperature	N, eV
U_d	Discharge voltage	V
V, V_s	Potential, probe potential	V
V_f	Floating potential	V
V_p	Plasma potential	V
v	Velocity	m/s
θ, θ_{div}	Longitude, Divergence angle	rad
x, y, z	Coordinates	m

I. Introduction

Measurements of electron parameters, i.e. electron density and temperature, in the plasma of electric propulsion devices for spacecraft is of great relevance as electrons govern to a large extent the properties and dynamics of the plasma discharge, and thus ultimately the performance and the lifetime of the system. Moreover, electrons define the thruster/spacecraft environment and play a key role in the ion beam neutralization process. An accurate and comprehensive knowledge about aforementioned quantities is then critical for the validation of plume modeling and numerical simulations, for improving thruster performances, for the study of facility effects and for understanding the interactions between the ejected plasma and the spacecraft elements.

This article deals with measurements performed by means of several cylindrical Langmuir probes in the near-field and far-field plasma plume of the 5 kW-class PPS®Dual Hall thruster. The thruster was fired with xenon and krypton as propellant in high-thrust / low-specific impulse regimes as well as in low-thrust / high-specific impulse regimes. Experiments were carried out in the PIVOINE-2G vacuum chamber in Orléans, France. In the downstream region of the plume, a Langmuir probe was installed on the rotating arm of the test-bench, in such a way quantities of interest could be acquired over a 200 ° circular arc. All measurement outcomes and associated quantities are presented and discussed in this article for a broad range of operating conditions with both xenon and krypton as fuel. The treatment of the Langmuir probe characteristic curves is especially examined along with the form of the electron energy distribution function $g(\varepsilon)$ as, to the best of our knowledge, there are only a few similar studies available in the open literature for high power Hall thrusters. The impact of the discharge voltage, gas mass flow rate, input power and propellant type upon the electron parameters is largely presented and commented here. The last section of the contribution is dedicated to the electron adiabatic exponent γ_e computed by combining density and temperature data. As expected, the value of the exponent is below the value of an atomic gas. But surprisingly, in the plume far-field the value of the exponent does not depend upon the angular position despite large variations in electron density and temperature with the angle. In the plume near-field, no value could be extracted, showing that γ_e is highly dependent on operating conditions.

II. Vacuum chamber and Hall thruster

A. The PIVOINE-2G test bench

Investigation of the high-power PPS®Dual Hall thruster plasma plume properties has been performed in the PIVOINE-2G test-bench at the ICARE laboratory in Orléans. This ground-test facility is fully dedicated to research and development activities in the field of Electric Propulsion.

PIVOINE-2G is a cryogenically pumped 4 m in length and 2.2 m in diameter stainless steel vacuum chamber. The bench allows testing Hall thrusters from 100 W up to 25 kW input power. The PIVOINE-2G test-bench was built in 1997 with the financial support of the French space agency CNES and the "Region Centre Council". It was upgraded in 2007 to achieve a pumping speed in excess of 250000 l/s, one of the largest within Europe. The current version is composed of two cryogenic stages optimized for xenon, although krypton and argon can also be efficiently evacuated. The cryogenic panels are shielded from the thruster thermal load and from the ion beam by means of LN_2 cooled graphite tiles. When using the two stages, a background gas pressure of 2×10^{-5} mbar can be achieved with 20 mg/s of xenon. A 2000 l/s-N_2 turbomolecular pump is also used for removal of light gases like hydrogen and helium. The vacuum chamber is equipped with a large lock-chamber that permits inserting the thruster without disturbing the vacuum as well as with different observation windows and diagnostic ports. PIVOINE-2G has a set of diagnostics that includes a thrust balance, ion current probes and an energy analyzer. The probes can be installed either on a 2D translation stage or on a rotating arm that allows performing measurements in a hemisphere. The thrust balance is a pendulum stand, calibrated in-situ with a series of weights. The estimated accuracy of the measured thrust is ±1 mN for a thrust ranging from 5 to 1500 mN. The discharge power is provided by two 500 V–30 A supplies mounted either in parallel or in series. During operation of a thruster, more than hundred parameters are monitored and continuously acquired. In 2019, the PIVOINE-2G bench control unit has been upgraded to allow fully automated operation and process. The facility is now able to operate on a 24 hour/7 day basis, which reduces cost and duration of endurance testings and open up the way to more ambitious experimental campaigns.

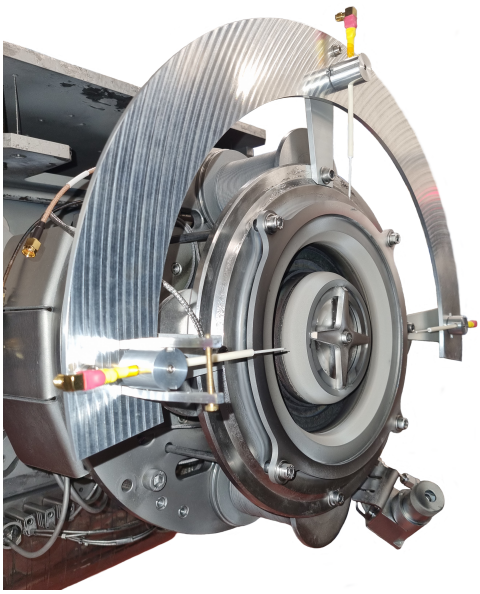

(a) PPS®Dual-EM thruster.

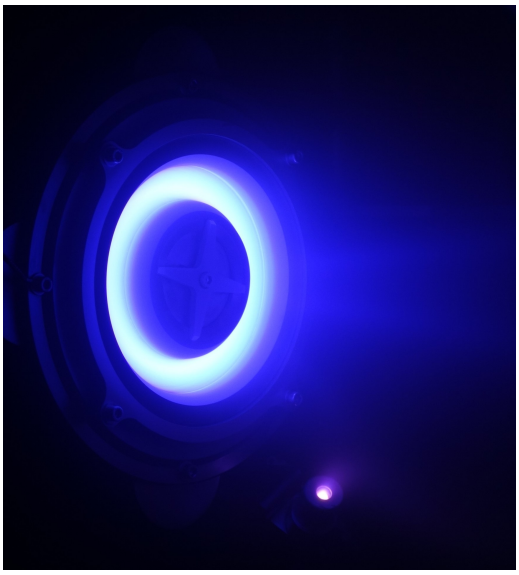

(b) PPS®Dual-EM thruster firing with krypton.

Figure 1. (a) Photograph of the high-power PPS®Dual-EM Hall thruster installed on the PIVOINE-2G test-bench thrust balance. Also visible are the three Langmuir probes with their holder placed near the channel exit plan. (b) Photograph of thePPS®Dual-EM Hall thruster firing with krypton in the PIVOINE-2G test-bench.

B. Hall thruster

1. *PPS® Dual thruster*

The PPS®Dual thruster is a 5 kW-class Hall thruster developed by SAFRAN. The PPS®Dual thruster is able to deliver both a large thrust level and a large specific impulse I_{sp} level at high power, up to 7 kW. The unique dual mode capability of the PPS®Dual rests upon a highly versatile magnetic configuration that inherits the experience gained with the PPS®1350, the PPS®5000 and the PPS 20k-ML thrusters over the last decade. A high thrust is for instance required for orbit raising and orbit transfer in order to reduce the maneuver duration. A large specific impulse is preferable for station keeping and trajectory corrections in the case of satellites. For cargo vehicles, space tugs and interplanetary missions a large I_{sp} makes it possible to considerably reduce the propellant mass and therefore increase the payload mass or extend velocity increment capacity. Two main input power targets have been initially proposed with xenon as fuel for the PPS®Dual thruster to cover aforementioned needs, namely: a 7 kW operating point for high thrust (0.5 N,$I_{sp} \geq 1800$ s, $T/P = 72$ mN/kW) and a 3.5 kW operating point for large specific impulse (0.2 N,$I_{sp} \geq 2100$ s, $T/P = 57$ mN/kW).

Two versions of the PPS®Dual thruster have been developed in the frame of the European CHEOPS project: a laboratory version, termed LM, and an engineering model, termed EM. In this work, the EM version was used with xenon and krypton as propellants. A photograph of the EM version of the PPS®Dual thruster is shown in Fig. 1a. As can be seen, the LaB_6 hollow cathode that furnishes the electron current for plasma discharge generation and ion beam neutralization is positioned under the thruster body. The thruster channel is dimensioned to warrant stable and efficient operation around 5 kW input power. Channel walls are made of boron-nitride ceramics (BN). The propellant gas is injected from the channel back through an annular graphite injector that also serves as anode. The magnetic field is created by a set of magnetizing coils (4 external coils,1 inner coil and 1 back coil) embedded into a pure iron magnetic circuit. The magnetic design gives a large flexibility in terms of shape and magnitude. Figure 1b shows the PPS®Dual-EM thruster in operation with krypton at 5 kW in the PIVOINE-2G test bench. As can be seen, the plasma discharge is concentrated in the ceramic channel. The cathode plasma plume is also visible in Fig. 1b.

Table 1. Operating conditions of the PPS®Dual-EM thruster for xenon.

Point	Φ_a	U_d	I_d	P	p	T	I_{sp}
-	mg/s	V	A	kW	10^{-5} mbar	mN	s
OP1	9.8	300	10	3	1.3	171	1788
OP2	7.0	400	7.5	3	1.0	147	2136
OP3	6.0	450	6.7	3	0.9	132	2251
OP4	15.5	300	16.7	5	2.0	284	1871
OP5	9.0	500	10	5	1.3	-	-
OP6	18.1	300	20	6	2.7	335	1886

Table 2. Operating conditions of the PPS®Dual-EM thruster for krypton.

Point	Φ_a	U_d	I_d	P	p	T	I_{sp}
-	mg/s	V	A	kW	10^{-5} mbar	mN	s
OP1	8.0	300	10	3	1.3	124	1580
OP2	6.0	400	7.5	3	1.1	117	1981
OP3	5.4	450	6.7	3	0.9	102	1925
OP4	12.2	300	16.7	5	1.9	217	1817
OP5	7.2	500	10	5	1.4	-	-
OP6	14.2	300	20	6	2.5	262	1881

2. Operating conditions

The PPS®Dual Hall thruster was operated over a broad range of discharge voltages and currents during the experimental campaigns. The current was kept identical for the two propellants by tuning the mass flow rate. The operating points are then similar for xenon and krypton in terms of voltage and input power. The cathode mass flow rate was set to 8 % of the anode flow rate for all conditions.

Six operating conditions have been selected for the Hall thruster in this study [OP1–OP6]. Operating parameters are listed in Tab. 1 for xenon and in Tab. 2 for krypton. The residual gas pressure, the measured thrust level and the anode specific impulse are also given in the tables.

III. Measuring instruments

A. Langmuir probes

Four cylindrical Langmuir probes were build to assess the electron properties as well as the local plasma potential in the plasma plume of the PPS®Dual Hall thruster, see.[1–8] Figure 2 shows the layout of the 4 Langmuir probes. Three probes, termed LP1 – LP3, are placed in the vicinity of the thruster channel exit plan at different azimuthal positions. The fourth probe, termed LP4, is placed in the far downstream region of the plasma plume 705 mm away from the channel exit plane. LP4 is mounted onto a rotating arm in order to perform measurements over a 200° circular arc. Note the LP4 probe is in the horizontal plan that contains the thruster centerline. The LP4 tip points towards the thruster axis. The pivot point of the rotating arm is in the thruster channel exit plan and aligned with the thruster axis. The exact position of the 4 probes are given in Tab. 3. As can be seen, LP1, LP2 and LP3 are placed at different axial positions.

The probe active part (tip) was made in tungsten in all cases. It was 0.5 mm in diameter and 25 mm in length for the probe placed in the far-field plume. The tip was 0.4 mm in diameter and 3 mm in length for the 3 probes placed near the channel exhaust, i.e. LP1, LP2 and LP3. The difference in geometry is due

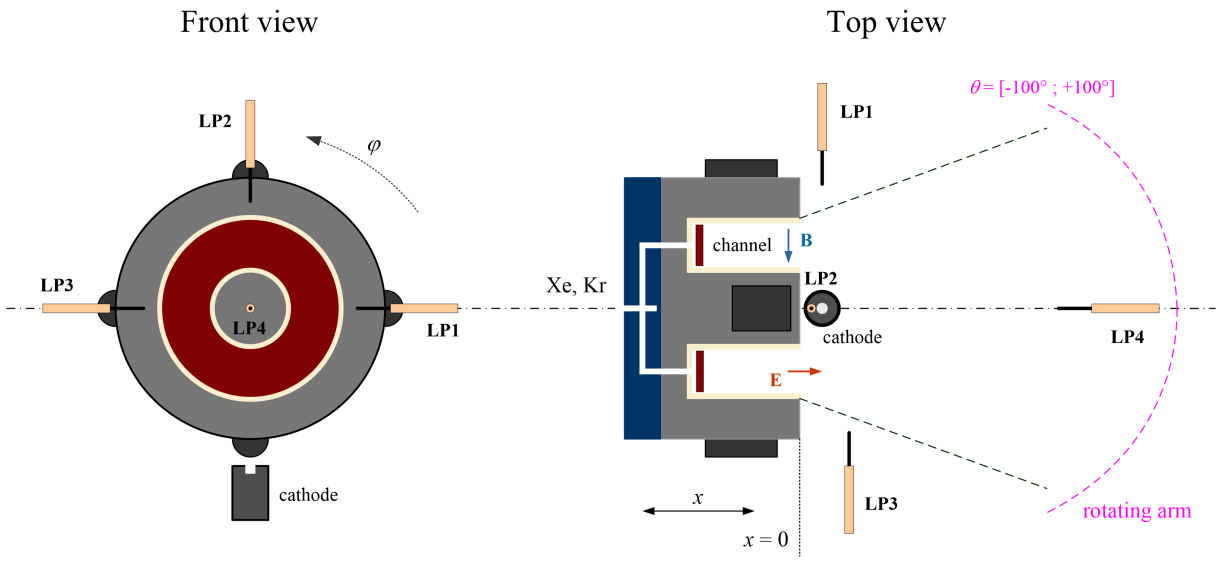

Figure 2. Layout of the 4 Langmuir probes. Not to scale.

to the large difference in Debye length and sheath sizes between the surveyed regions.[9–14] The non-active section of the W wire was shielded from the plasma with a 1.5 mm outer diameter alumina tube inserted into a shorter 2 mm inner diameter alumina tube, as illustrated in Fig. 1a. The total length of the probes was 100 mm. A 50 omhs coaxial cable was used to polarized the probe and collect the current. An ALP system^{TM} unit manufactured by Impedans Ltd was used to control the sweep of the probe voltage V_s and to measure and record the current. The voltage stepsize was set to 0.5 V for all data acquisitions.

As previously mentioned, LP4 was mounted onto a dedicated holder fixed to the PIVOINE-2G vessel rotating arm. A CAD image of the holder is given in Fig. 3. As can be seen, the Langmuir probe angular position does not coincide with the one of the rotating arm, hence making the measuring device asymmetrical. In other words, when the arm is placed at $\theta_{arm} = 0°$, the probe is at another angular position. The angle between the two probes is +15°.

Figure 3. CAD image of the LP4 Langmuir probe setup. The LP is not aligned with the rotating arm.

B. Current–Voltage curves

Figure 4 shows the current-voltage characteristic curves recorded with LP4 in the plasma plume far-field of the PPS®Dual Hall thruster at two angles, namely 0° (thruster axis) and +80° (plume edge). The thruster functioned in OP3 (450 V, 3 kW). Figure 5 shows I-V curves obtained under similar conditions with krypton as fuel. The Langmuir probe voltage was swept from -20 V to +40 V in all cases. A cubic spline function has been used to interpolate the raw data, therefore increasing the number of points for data treatment.

Table 3. Langmuir probe position.

Quantity	LP1	LP2	LP3	LP4
		Near field		Far field
x	11 mm	19 mm	29 mm	705 mm
y[a]	9.5 cm	9.5 cm	9.5 cm	-
φ, θ	0°	90°	180°	-100° / + 100°

[a] wrt the thruster centerline

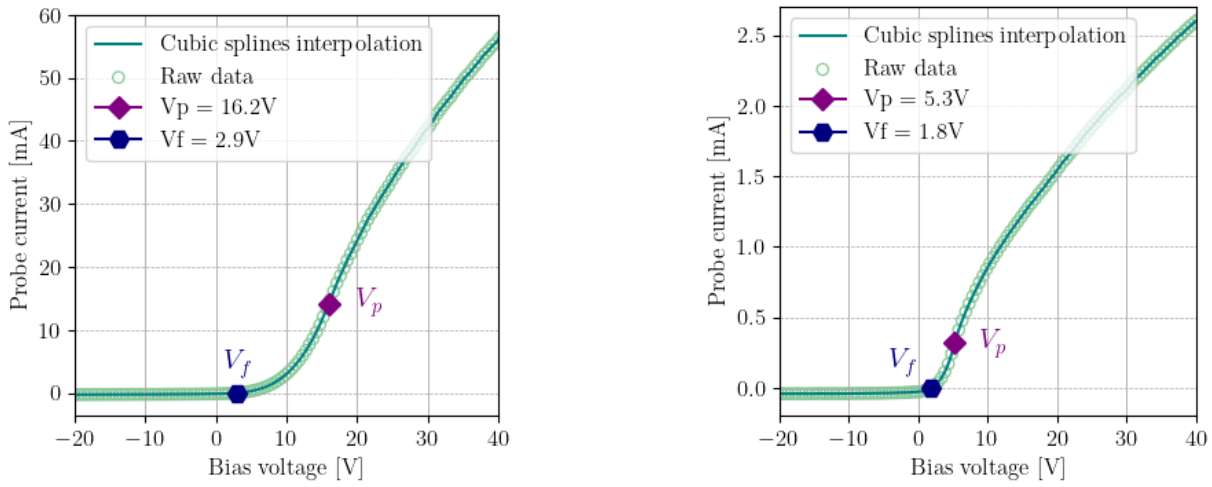

(a) Xenon, OP3, 0°

(b) Xenon, OP3, 80°

Figure 4. (a) I-V curve measured with LP4 in OP3 at $\theta = 0°$ when the thruster fires with xenon. (b) I-V curve measured with LP4 in OP3 at $\theta = +80°$ when the thruster fires with xenon.

The value of both the floating potential V_f and the plasma potential V_p are also given in Fig. 4 and Fig. 5. By definition, a probe that is electrically floating collects no net current from the plasma. The floating potential of a Langmuir probe is then the potential at which ion and electron currents cancel each other out, i.e. there is no net current. The part of the curve below V_f is termed the ion branch: only ions are collected, electrons being repelled. The section of the I-V curve above V_f is the electron branch: only electrons are attracted. The plasma potential is obtained from the maximum of the first derivative of the probe I-V characteristic:

$$V_p = max\left(\frac{dI}{dV_s}\right). \tag{1}$$

The plasma potential corresponds to the inflection point (knee) of the I-V curve. It indicates the transition between the exponential growth region and the electron saturation region where plasma sheath effects dominate.[9–14] As can be seen in Fig. 4 and Fig. 5, V_f is positive, as expected for a electropositive plasma confined in a grounded chamber. V_p is around 15 V on-axis for the two gases and it decreases with the angle.

C. EEDF

The electron energy distribution function (EEDF) refers to the probability density function that describes the energy distribution of electrons within a plasma.[1,2,15–20] The EEDF provides valuable information about the population of electrons at different kinetic energies or velocities. The shape of the EEDF determines the

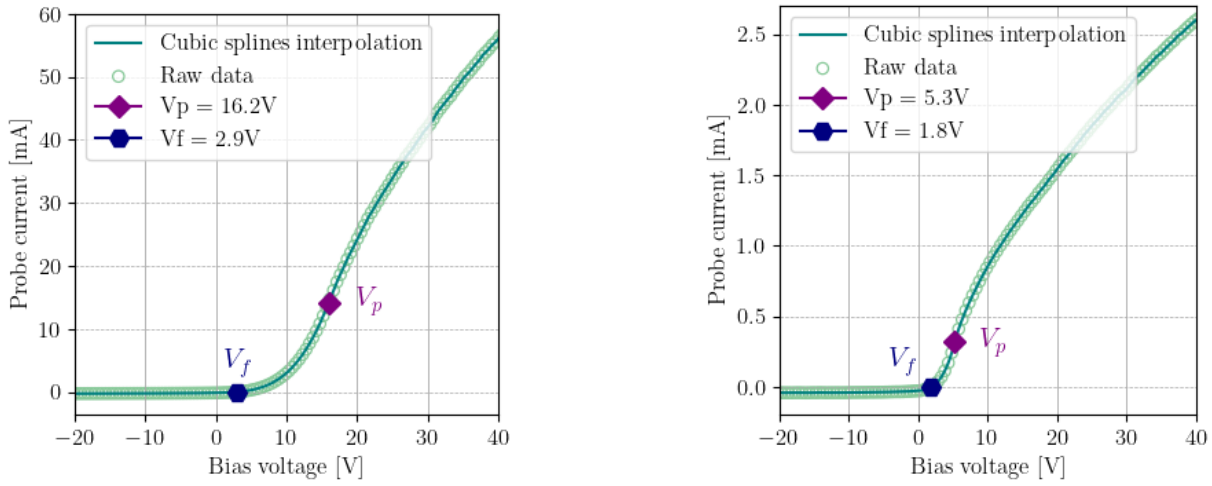

(a) Krypton, OP3, 0°

(b) Krypton, OP3, 80°

Figure 5. (a) I-V curve measured with LP4 in OP3 at $\theta = 0°$ when the thruster fires with krypton. (b) I-V curve measured with LP4 in OP3 at $\theta = +80°$ when the thruster fires with krypton.

behaviour of electrons within the plasma. Understanding the EEDF allows to identify the dominant energy transfer (heating and cooling) mechanisms at play.

Assuming an isotropic plasma and a convex small probe, the EEDF $g(\varepsilon)$ is related to the second order derivative of the electron current I_e with respect to the probe voltage according to the following expression, the so-called Druyvesteyn relation:

$$\frac{d^2 I_e(V_s)}{dV_s^2} = \frac{e^3 A}{2\sqrt{2m_e}} \frac{g(e(V_p - V_s))}{\sqrt{e(V_p - V_s)}} = \frac{e^3 A}{2\sqrt{2m_e}} \frac{g(\varepsilon)}{\sqrt{\varepsilon}}, \tag{2}$$

where ε is the electron kinetic energy that reads $\varepsilon = \frac{1}{2} m_e v_e^2 = e(V_p - V_s)$. Note that the electron current I_e must be taken over the interval minus infinity ($V_s < V_f$) to V_p. High energy electrons are collected around V_f while very low-energy electrons are captured at V_p. The associated electron energy probability function EEPF $\hat{g}(\varepsilon)$ is given by:

$$\hat{g}(\varepsilon) = \frac{g(\varepsilon)}{\sqrt{\varepsilon}}. \tag{3}$$

For a Maxwellian EEDF, the EEPF is a straight line in a semilog plot, hence the importance.

Figure 6a and 6c show the EEPF computed from the measured I-V curve when the PPS®Dual Hall thruster operates with xenon in OP5 for two different angles. Figure 6b and 6d show the EEPF computed from the measured I-V curve when the thruster operates with krypton in OP5 for two angular positions. The raw I-V trace has been interpolated with a cubic spline function and smoothed with a second order Savitzky-Golay filter before computing the second order derivative.[21] Note that the ion current was not substracted to the measured total current I. Therefore we make the assumption:

$$\frac{d^2 I_e(V_s)}{dV_s^2} \approx \frac{d^2 I(V_s)}{dV_s^2}. \tag{4}$$

Since the evolution of ion current with probe voltage is almost linear, this assumption is reasonable. The error produced is around V_f. It therefore affects the high energy part of the EEDF and EEPF.

In Figures 6, the red line corresponds to a Maxwellian distribution, i.e. an equilibrium distribution. The green line is a Druyvesteyn distribution.[15,18–20,22] Information about these two types of EEDF can be found in appendix A. The EEPF is clearly is in non-equilibrium for the two gases, that means it deviates from a Maxwellian distribution. This is observed for all angles and all operating conditions in this work. The high energy tail of the measured distribution is depleted above the ionization energy. In such cases, the EEDF is

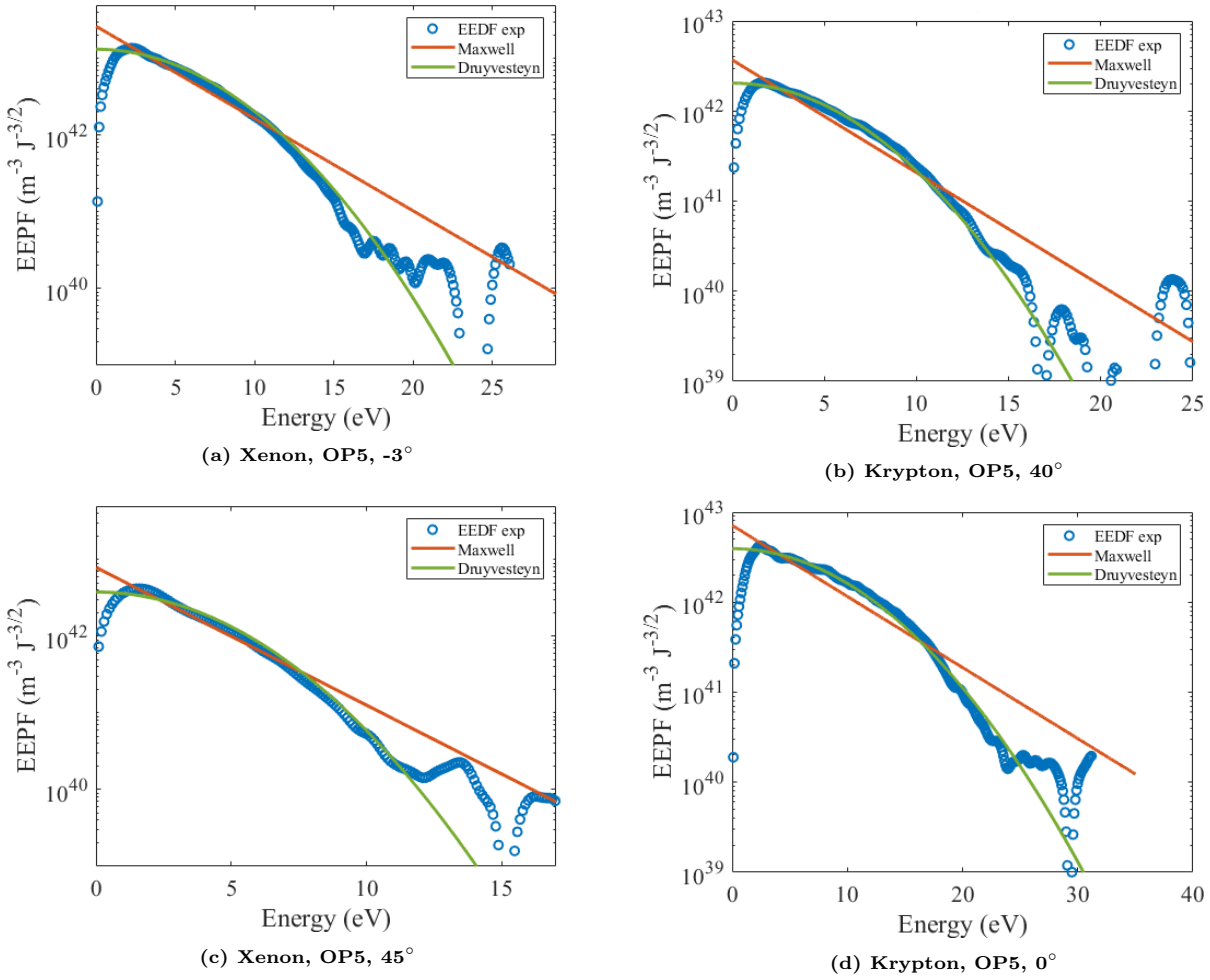

(a) Xenon, OP5, -3°

(b) Krypton, OP5, 40°

(c) Xenon, OP5, 45°

(d) Krypton, OP5, 0°

Figure 6. (a) EEPF at $\theta = -3°$ when the thruster fires with xenon. (b) EEPF at $\theta = 40°$ when the thruster fires with krypton. (c) EEPF at $\theta = 45°$ with xenon. (d) EEPF at $\theta = 0°$ with krypton. OP5 for all measurements. Also shown is a fit with a Maxwellian distribution (red line) and with a Druyvesteyn function (green line).

often described as the sum of two or more Maxwellian distribution covering several energy ranges. However, as can be seen in Fig. 6, the EEPF is perfectly described by a Druyvesteyn distribution. Instead of using a constant elastic collision frequency (inelastic collisions are neglected), like in the Maxwellian EEDF, the Druyvesteyn EEDF assumes a constant, electron-energy-independent cross section. This leads to a drop of the EEDF at high electron energies for the same mean electron energy.

The drop observed for the measured EEPF at very low electron energies has two main origins: the uncertainty on the value of the plasma potential and the finite resistance of the probe circuit R_c.[17,23] It is present in most, if not all, studies that involve Langmuir probes. It leads to a small underestimate of the electron density. To avoid, or at least minimize, the drop, the load of the electrical circuit associated with the probe has to be much smaller than the plasma resistance R_{plasma}. Typically one needs $R_c < 0.01 R_{plasma}$. The plasma resistance is given by:

$$R_{plasma} = \frac{T_e}{I_{e,sat}}. \tag{5}$$

As an example the plasma resistance in the plume of the PPS®Dual thruster is about 350 Ω on-axis and 4200 Ω at 80° in OP3 with xenon.

D. Electron parameter determination

1. Electron density

When the voltage applied to the probe reaches V_p, the sheath around the probe disappears. At this point, the collection surface corresponds to the geometric surface of the probe tip, and the measured current corresponds to the thermal flux. Therefore, the electron density can be obtained by measuring the electron current I_e at V_p using the following formula:

$$I_e = An_e\sqrt{\frac{e^3T_e}{2\pi m_e}}, \tag{6}$$

The accuracy of this method is often criticized. A slight shift in V_p significantly impacts the electron density. However, this method provides an estimate of the trend and the order of magnitude. The electron density n_e can also be extracted from the Electron Energy Distribution Function, $g(\varepsilon)$. By definition it is given by the integral of the EEDF over all energies:

$$n_e = \int_0^\infty g(\varepsilon)d\varepsilon = \int_0^\infty \sqrt{\varepsilon}\hat{g}(\varepsilon)d\varepsilon. \tag{7}$$

In a collisionless plasma, when the sheath thickness is greater than the probe radius, the collection of charged particles is governed by orbital motion.[3,24–26] Assuming an isotropic Maxwellian electron velocity distribution function, the Orbital Motion Limited (OML) model provides an equation that relates the ion saturation current to the ion density for a cylindrical Langmuir probe:

$$I_i = 2\pi r_p l e n_e \frac{\sqrt{2}}{\pi}\sqrt{\frac{k_BT_i}{m_i}}\sqrt{1+\frac{e(\pm V \pm V_p)}{k_BT_i}}, \tag{8}$$

where l is the length of the probe active part and r_p its radius. In the OML regime, the slope S of the I_i^2 versus V_s plot is proportional to n_i^2:

$$S = \frac{2}{m_i\pi^2}A^2e^3n_i^2. \tag{9}$$

The electron density is obtained assuming quasineutrality of the plasma: $n_e \approx n_i$. The OML approach is interesting as it eliminates the need to calculate V_p and T_e, therefore reducing uncertainties.

2. Electron temperature

The electron temperature is determined from the slope of the logarithm of the electron current in the transition region between V_f and V_p as the current increases exponentially with the voltage applied to the probe when the EEDF is assumed to be a Maxwellian distribution:

$$T_e = \left(\frac{d(Ln(I_e)}{V_s}\right)^{-1}. \tag{10}$$

Here the ion current was not substrated to the total current, so we used $Ln(I)$ instead of $Ln(I_e)$.

The temperature can also be determined directly from the EEDF. The normalized first order moment of the EEDF gives the average electron kinetic energy $\langle\varepsilon\rangle$:

$$\langle\varepsilon\rangle = \frac{1}{n_e}\int_0^\infty \varepsilon g(\varepsilon)d\varepsilon. \tag{11}$$

Subesequently an effective electron temperature can be calculated from $\langle\varepsilon\rangle$:

$$T_{eff} = T_e = \frac{2}{3}\langle\varepsilon\rangle. \tag{12}$$

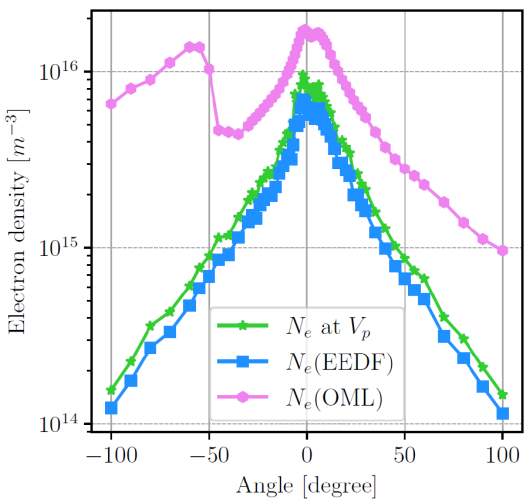

(a) Xenon, OP3, n_e

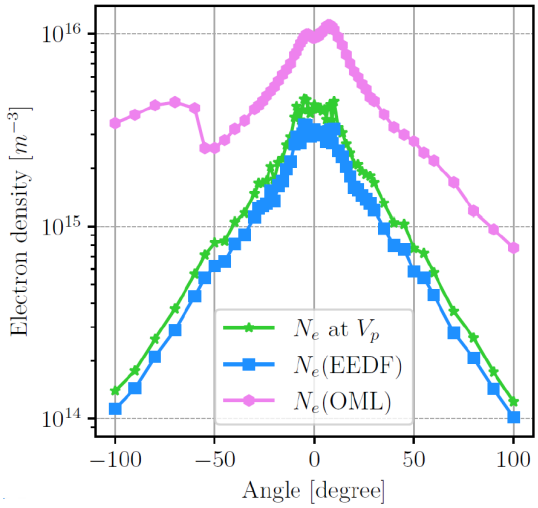

(b) Krypton OP3, n_e

Figure 7. (a) Electron density angular profile in OP3 when the thruster fires with xenon. (b) Electron density angular profile in OP3 when the thruster fires with krypton. The electron density has been calculated with the three methods explained in section III D.

IV. Electron parameters in the plume far-field

A. Electron density angular profiles

Figures 7a and 7b show the angular distribution of the electron density in the far-field of the plasma plume when the PPS®Dual Hall thruster is firing at OP3 with xenon and krypton, respectively. The density has been determined by means of the three methods described in section III D. As expected the density is the largest on-axis and it decreases fast when the angle increases. The density is larger for xenon as the latter has a relatively low ionization energy. The thin sheath approach and the method based on the EEDF give about the same values for n_e whatever the angle and the gas. On the contray, the calculation performed with the OML theory gives a much larger density both for xenon and krypton even though the trend remains the same.

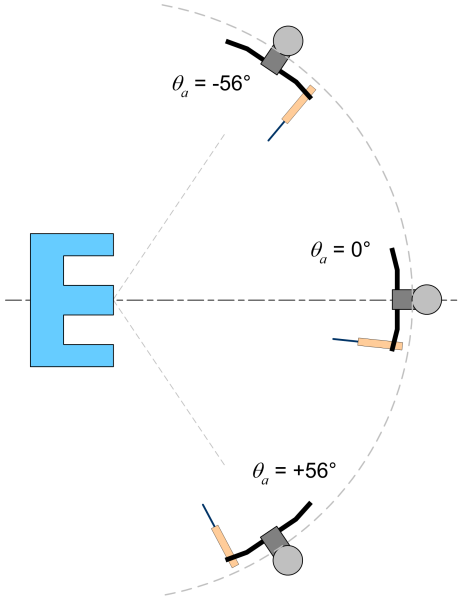

Figure 8. Representation of the asymmetry introduced by Langmuir probe LP4 in the plume far-field.

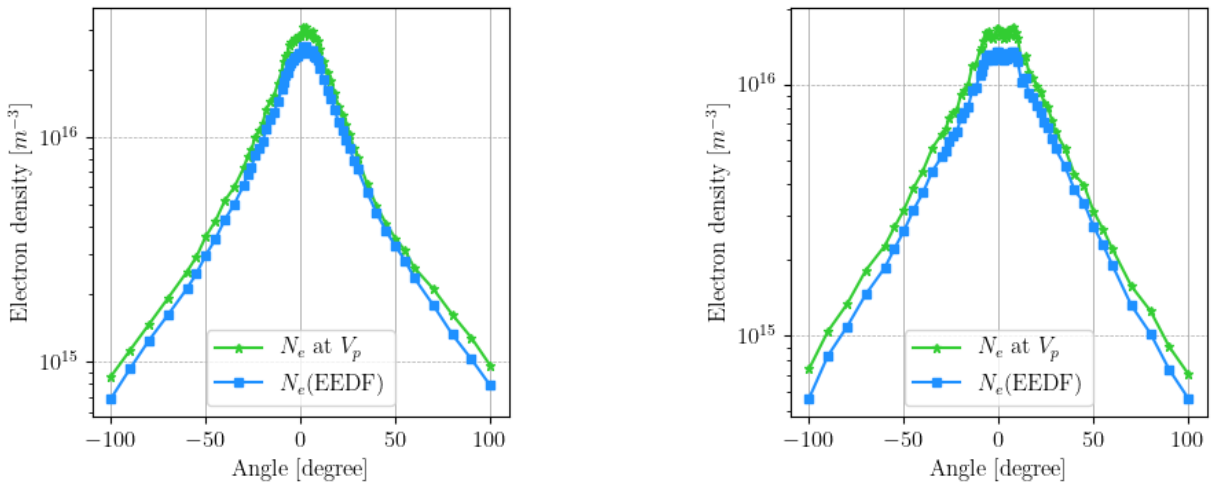

(a) Xenon, OP6, n_e

(b) Krypton OP6, n_e

Figure 9. (a) Electron density angular profile in OP6 when the thruster fires with xenon. (b) Electron density angular profile in OP6 when the thruster fires with krypton. The electron density was calculated using the thin sheath theory and the EEDF.

Moreover, in Fig. 7 one can observed an anomaly for negative angles: a bump is visible on the angular profile beyond -50 degrees. The bump is always present with the OML model whatever the operating conditions. The anomaly remains difficult to explain at this point. We believe the anomaly is a consequence of an asymmetrical probe device. As illustrated in Fig. 3, the Langmuir probe (LP4) is not aligned with the rotating arm of the PIVOINE-2G bench. The misalignment makes the interaction between the ion beam, the arm and the probe, and the resulting perturbation, asymmetrical as exemplified in Fig. 8. For positive angles, the probe sees the low-density region of the plume with respect to the arm radius, whereas for negative angles it sees the high-density region. Recall that OML theory involves the ionic branch of the I-V curve. Therefore in the remainder of this article, OML theory will not be used to determine electron density.

Note that the asymmetry in the n_e angular profile is not observed when, in the OML model, the ion current is replaced by the electron current. This fact support the idea that the asymmetry is caused by the interaction between the probe system and the ion flux.

Figures 9a and 9b show the angular distribution of the electron density in the far-field of the plasma plume when the PPS®Dual Hall thruster is firing at OP6 with xenon and krypton, respectively. The density has been determined using the thin sheath theory (I_e at V_p) and the EEDF. The density is larger in OP6 compared to OP3 as it is the high current condition (300 V, 20 A). The density is larger for xenon. The thin sheath method gives a density slightly larger for all angles in OP3 and OP6 but the gap is small.

The difference between the center of the plume and the wings is practically two orders of magnitude for all conditions.

B. Electron temperature angular profiles

Figures 10a and 10b show the angular distribution of the electron temperature in the far-field of the plasma plume when the PPS®Dual Hall thruster is firing at OP3 with xenon and krypton, respectively. The temperature has been determined using the slope of the $Ln(I_e) - V_s$ curve and the EEDF. As expected the temperature is the largest on-axis and it decreases when the angle increases. The temperature is larger for krypton as its ionization energy is larger. The method based on the slope gives a much lower temperature whatever the angular position. The difference could have two origins, namely: the fact that the EEDF is not a Maxwellian and the hypothesis that $I_e \approx I$ around V_f.

Figures 11a and 11b show the angular distribution of the electron temperature in the far-field of the plasma plume when the PPS®Dual Hall thruster is firing at OP6 with xenon and krypton, respectively. The temperature has been determined using the slope of the $Ln(I_e) - V_s$ curve and the EEDF. The temperature

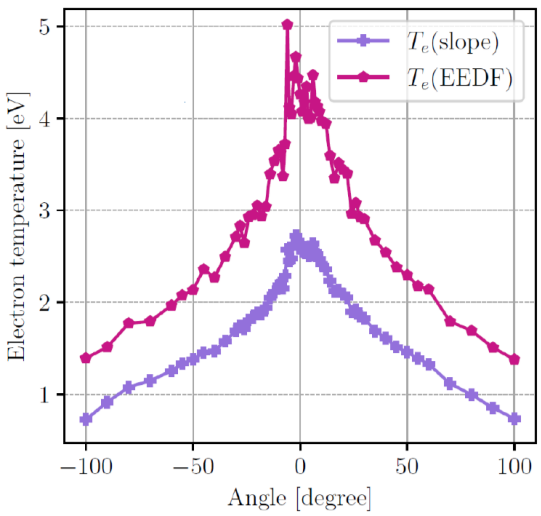

(a) Xenon, OP3, T_e

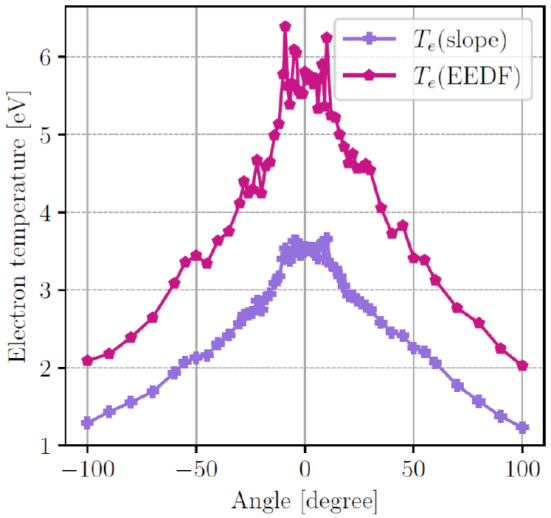

(b) Krypton OP3, T_e

Figure 10. (a) Electron temperature angular profile in OP3 when the thruster fires with xenon. (b) Electron temperature angular profile in OP3 when the thruster fires with krypton. The electron temperature was calculated using the slope of the $Ln(I_e) - V_s$ curve and the EEDF.

is the lower in comparison with measurements carried out in OP3 as here the applied voltage is lower and the current higher. The temperature is still larger for krypton due the ionization energy gap. The method based on the slope gives a much lower temperature whatever the angular position. What is noticeable in Fig. 11 is the asymmetry of the angular distribution. This is especially visible when T_e is determined using the slope: The distribution is broad and not center at $\theta = 0°$. This is probably due to heating of the Langmuir probe system as the input power reaches 6 kW in OP6. Heating changes the probe resistance as well as the secondary electron emission, which can disturb the measurement and lead to an erroneous I-V curve.

Two examples of EEPF measured in OP6 with th thruster firing with xenon are presented in Fig. 12. As can be seen the EEPF is close to a Maxwellian distribution even at low angles. For large angles the EEPF stays Maxwellian for low energie but for energies above the ionization potential, the tail of the distribution

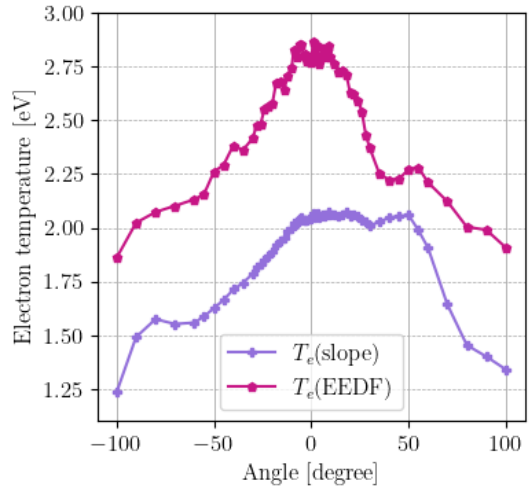

(a) Xenon, OP6, T_e

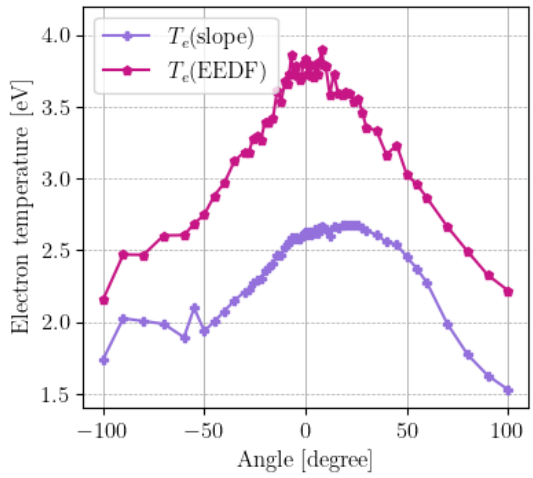

(b) Krypton OP6, T_e

Figure 11. (a) Electron temperature angular profile in OP6 when the thruster fires with xenon. (b) Electron temperature angular profile in OP6 when the thruster fires with krypton. The electron temperature was calculated using the slope of the $Ln(I_e) - V_s$ curve and the EEDF.

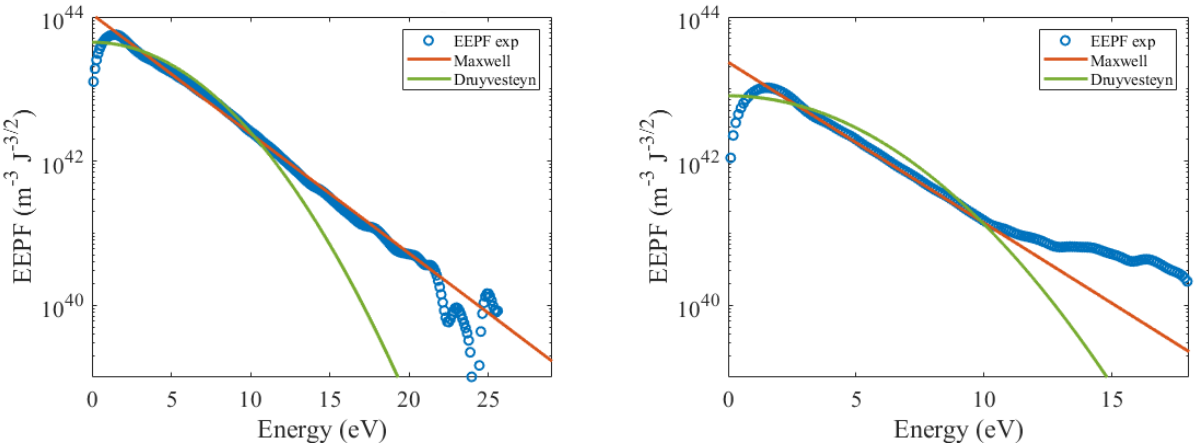

(a) Xenon, OP6, 0° **(b) Krypton, OP6, 50°**

Figure 12. (a) EEPF at $\theta = 0°$ and (b) EEPF at $\theta = 50°$. The thruster fires with krypton in OP6. Also shown is a fit with a Maxwellian distribution (red line) and with a Druyvesteyn function (green line).

is overpopulated. Two hypotheses can then be put forward: either there is a second population of high-energy electrons with a larger temperature, or the measurement is disturbed by the high current in the plume (heating of the probe). Further experiments are needed to decide between the two hypotheses.

C. Debye lenght and sheath thickness

The Debye length is given by the following relation when ions are assumed at rest and cold ($T_i = 0$):[27,28]

$$\lambda_D = \sqrt{\frac{\varepsilon_0 T_e}{e n_e}}, \tag{13}$$

where T_e is expressed in eV and ε_0 is the permittivity of free space. The floating sheath thickness s_{flot} is related to the Debye length according to the formula:[12,14,29]

$$s_{flot} = \frac{5}{\sqrt{h}} \lambda_D, \tag{14}$$

where $h = \exp(-0.5) \approx 0.6$ is a parameter that connects the electron density in the bulk of a plasma to the density at the edge of the sheath.[28] Finally, the high-voltage sheath thickness s_{hv} that corresponds to the sheath thickness when a potential larger than $|V_f|$ is applied to the probe, reads:[9,28,30,31]

$$s_{hv} = \frac{\sqrt{2}}{15} \left(\frac{2V_s}{T_e} \right)^{3/4} s_{flot}. \tag{15}$$

Here the plasma is collisionless, ions are cold and they enter the sheath with a kinetic energy well below the applied potential. The last assumption is not valid in the plume of a Hall thruster. Models do exist to take into account fast ions, see e.g.[31,32] High energy ions in fact increase the size of the plasma sheath.

Figure 13 shows the Debye length, floating sheath and high-voltage sheath (for 30 V) angular distribution computed for xenon and krypton in the far-field plume of the PPS®Dual Hall thruster firing in OP5 (500 V and 10 A). Quantities have been calculated with n_e and T_e obtained using the EEDF. The three quantities increase when the angle increase, that means the minimum is reached on-axis. The Debye length is in the 100s μm range and the two sheath thickness are in the mm range for the two gases. On the plume centerline, the probe radius r_p (0.25 mm) is in the order of the floating sheath thickness and larger than the Debye length, see section III. Charge carrier move in collisionless regime and the thin sheath theory holds. Off-axis of the plasma plume the probe radius is in the order of the Debye length and smaller than the floating sheath thickness. Charge carrier move in collisionless regime, the thick sheath theory applies and the Orbital Motion Limited (OML) model can be used. At any angle the Debye length and the sheath thickness are smaller than the length of the Langmuir probe (25 mm), therefore the probe can be considered as a cylindrical probe.

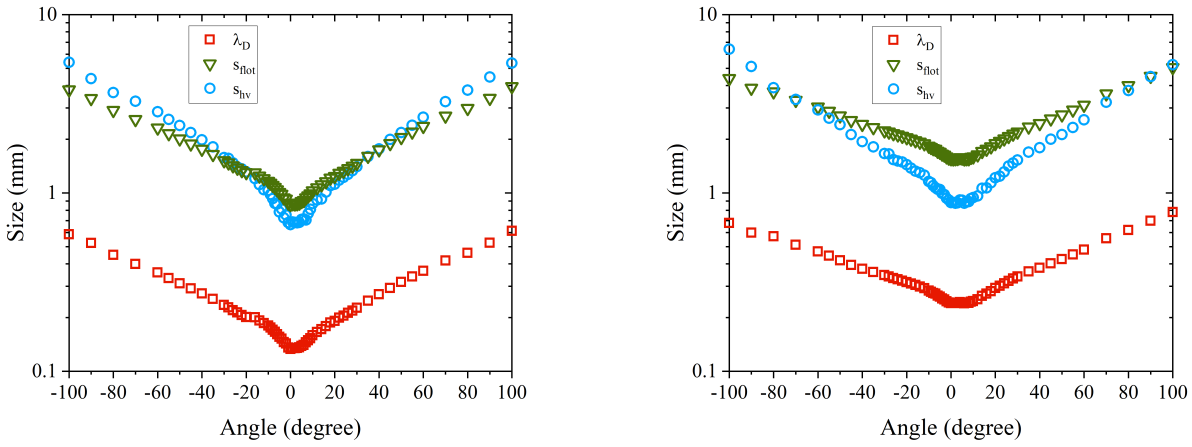

(a) Xenon, OP5 **(b) Krypton, OP5**

Figure 13. Debye length, floating sheath and high-voltage sheath (30 V) computed for xenon (a) and krypton (b) in the far-field plume of the PPS®Dual thruster fired in OP5.

D. Adiabatic exponent

The expansion of a plasma into a vacuum can often be considered as a steady expansion. The flow which is initially in thermodynamic equilibrium can be assumed to be adiabatic and if the flow is laminar, the expansion is isentropic. For a steady isentropic flow, the energy conservation equation can be replaced by the simple Poisson adiabatic relation, which is a polytropic state equation, when the electron gas is assumed to follow the perfect gas law:

$$\left(\frac{n_e}{n_0}\right)^{\gamma-1} = \frac{T_e}{T_{e,0}}, \tag{16}$$

where γ is the specific heat ratio (heat capacity at constant pressure c_p divided by the heat capacity at constant volume c_V) or adiabatic exponent and $n_{e,0}$ and $T_{e,0}$ are reference electron density and temperature respectively.[33] Note that when $\gamma = 1$ the plasma is isothermal, i.e. T_e remains constant. For an atomic gas, the adiabatic exponent is 5/3. For an electron fluid, the measured value of γ_e is below 5/3. In the literature, values typically range from 1.1 to 1.4 for Hall thrusters and magnetic nozzles, see e.g.[34–40] and references herein.

Figures 14 and 15 show the Log(T_e) versus Log(n_e) plots for all operating conditions when the PPS®Dual Hall thruster is fueled with xenon and krypton. The electron temperature and density are obtained from the EEDF, as previously explained. An (n_e,T_e) pair here refers to a certain angular position θ: $[n_e(\theta), T_e(\theta)]$. As can be seen, the experimental data follow a straight line, that means the plasma plume of a high-power Hall thruster can be considered as an adiabatic expansion in a vacuum, in the same way as medium-power thrusters.[34] In Fig. 14 and Fig. 15, low values of Log(n_e) correspond to large angles and large values of Log(n_e) correspond to small angles. Therefore there is no impact of the angle on the $[n_e(\theta), T_e(\theta)]$ pair distribution whatever the operating points in spite of large gradients between the core of the plasma plume and the edges, as exemplified in sections IVA and IVB.

The adiabatic exponent γ_e can be retrieved from the slope of the Log(T_e) versus Log(n_e) relationship, according to Eq. 16. Results obtained from the linear regression displayed in Fig. 14 and 15 are summarized in Tab. 4 for all operating conditions and the two propellants. The mean value of γ_e in the plasma plume, which accounts for all conditions, is 1.21 for xenon and 1.26 for krypton. It always stays below 5/3 and it is higher for krypton. Furthermore, γ_e increases with the discharge voltage U_d for a constant input power and it decreases with the propellant mass flow rate Φ_a, or the discharge current I_d, for a constant U_d.

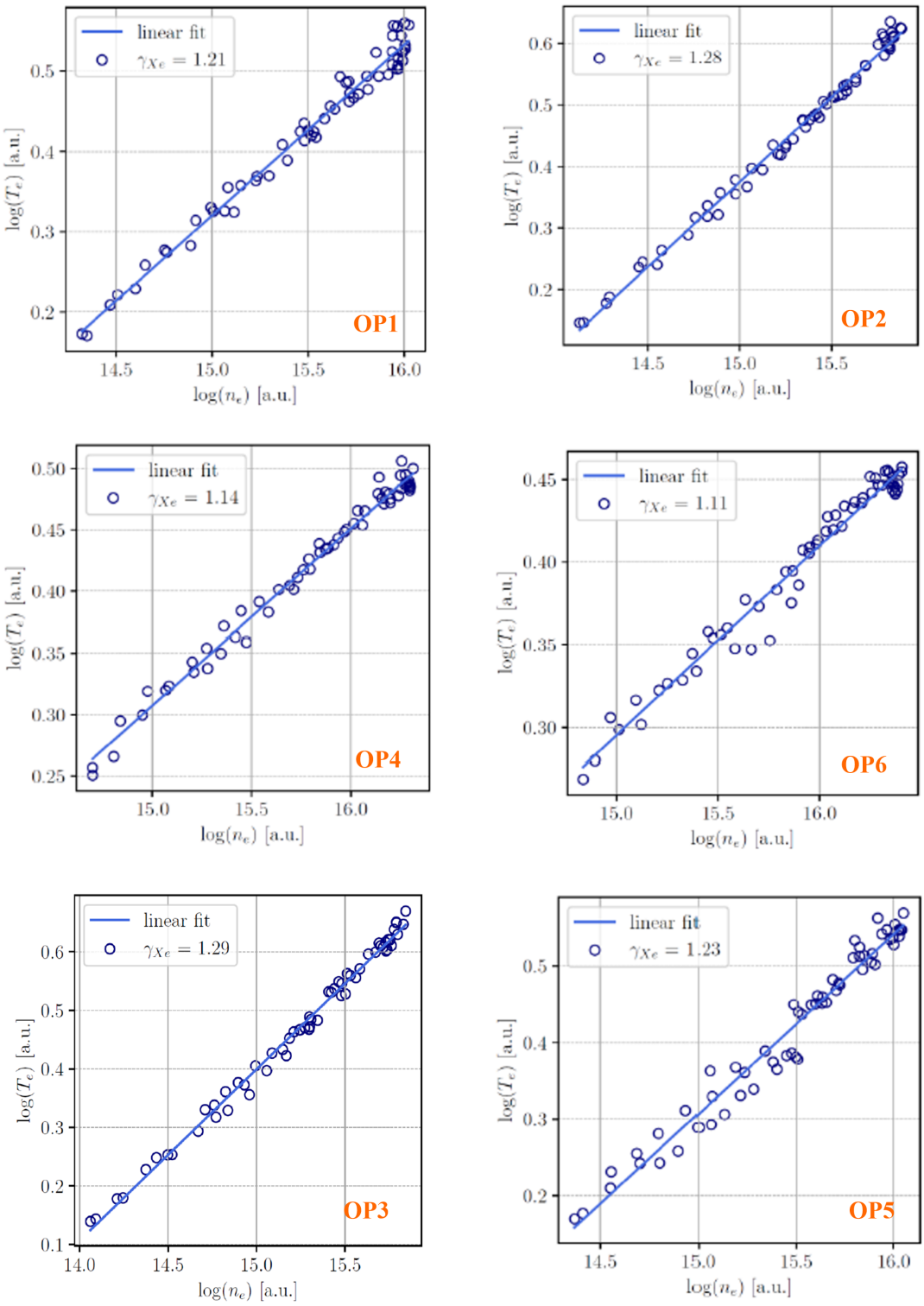

Figure 14. Log(T_e) against Log(n_e) plot for xenon in all operating conditions. The value of γ_e is given for each plot.

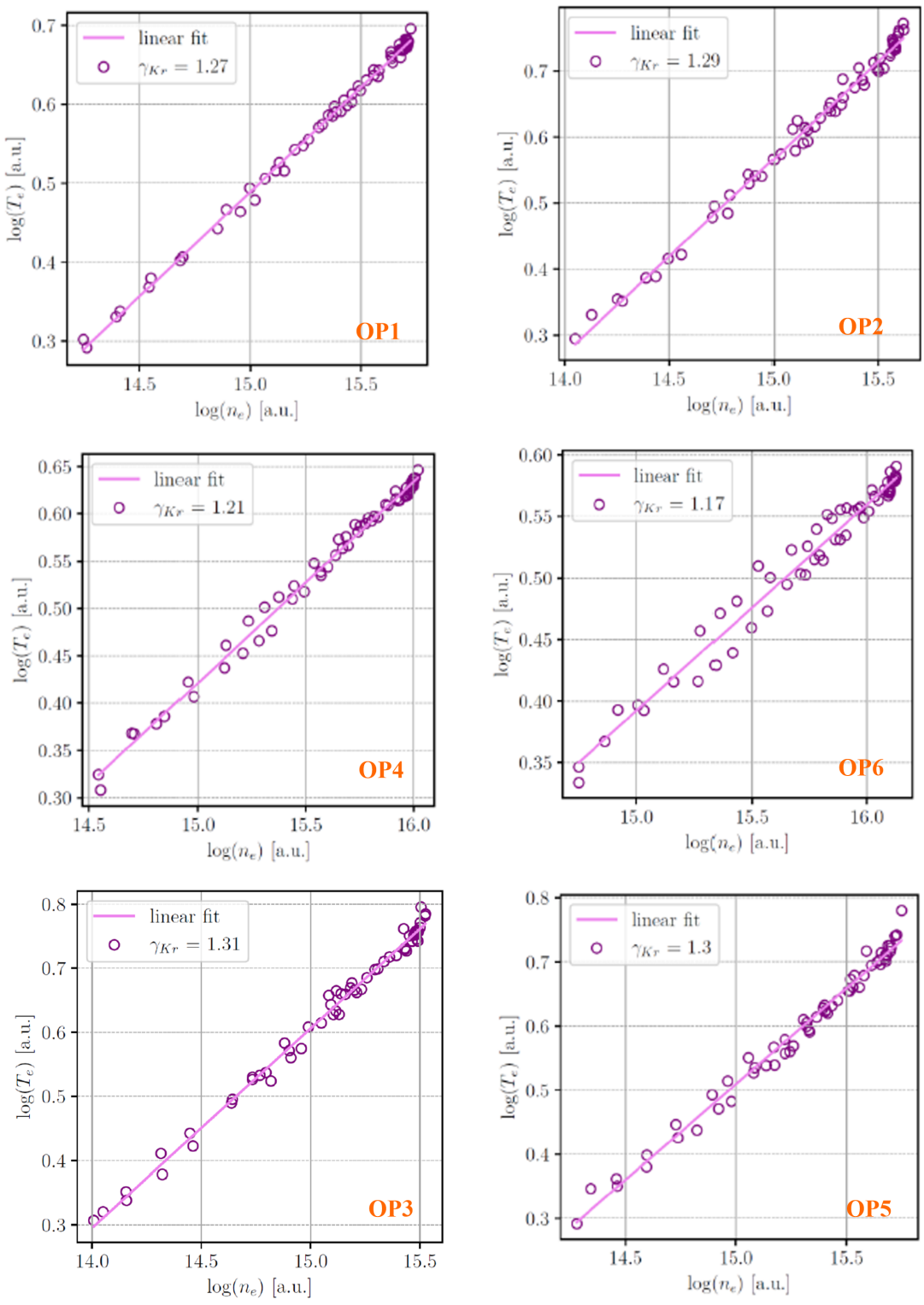

Figure 15. Log(T_e) against Log(n_e) plot for krypton in all operating conditions. The value of γ_e is given for each plot.

Table 4. *Electron adiabatic exponent γ_e for xenon and krypton for all operating points.*

Operating condition				Adiabatic exponent γ_e	
OP	Id (A)	U_d (V)	P kW	Xe	Kr
1	10	300	3	1.21	1.27
2	7.5	400	3	1.28	1.29
3	6.7	450	3	1.29	1.31
4	16.7	300	5	1.14	1.21
5	10	500	5	1.23	1.30
6	20	300	6	1.11	1.17
Mean value				**1.21**	**1.26**

In a nutshell, the adiabatic exponent γ_e is independent of the angular position in the far-field of the plume of the PPS®Dual Hall thruster, nevertheless it depends on the operating conditions and on the nature of the propellant supplied through the gas injector. The evolution of γ_e with the OPs and the gas nature is certainly of great interest. A better understanding of the physical phenomena involved (ionization, heat transfer...) will require further investigations, additional experiments and probably numerical simulations.

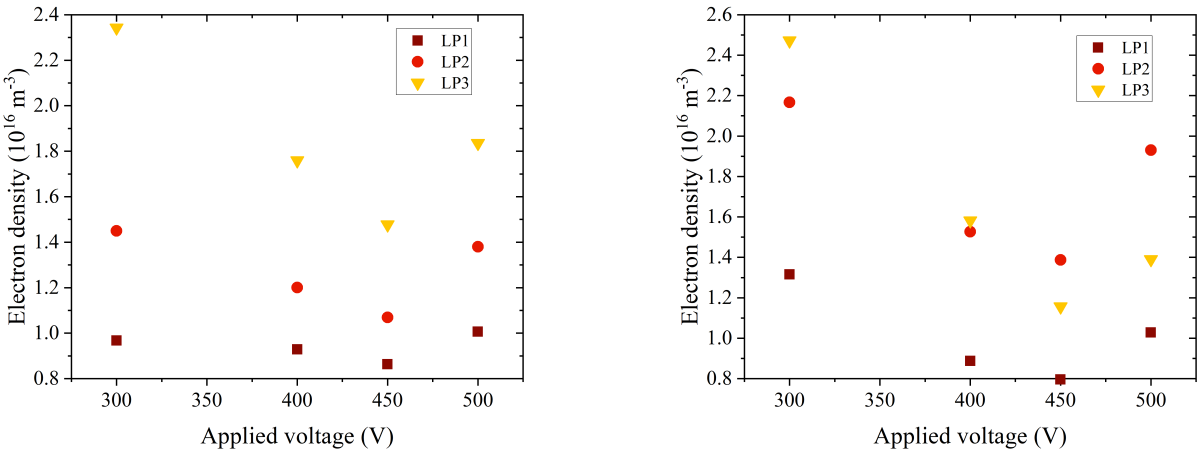

(a) Electron density, xenon

(b) Electron density, krypton

Figure 16. Electron density as a function of the discharge voltage measured with the three probes in the plume near-field. The density is computed from the EEDF. (a) Xenon. (b) Krypton.

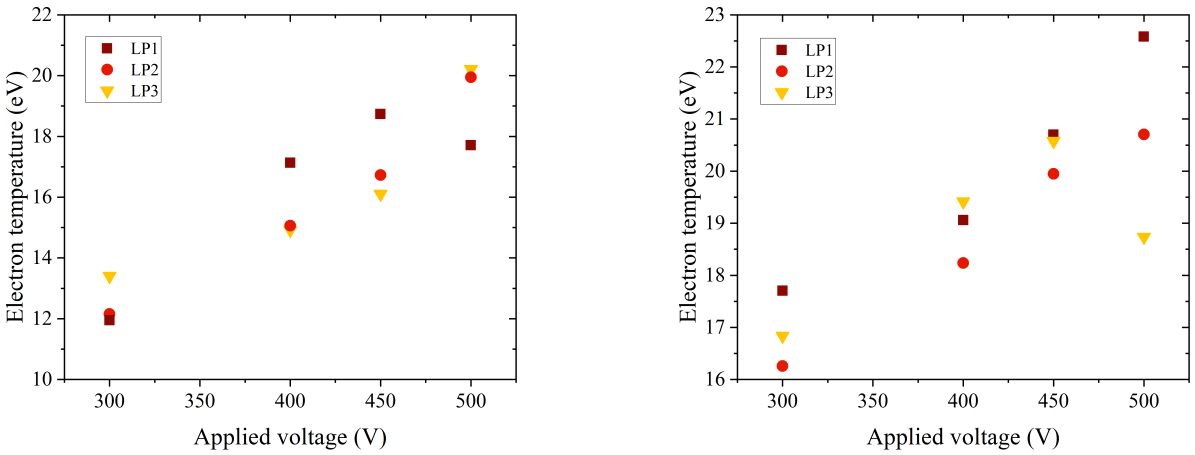

(a) Electron temperature, xenon

(b) Electron temperature, krypton

Figure 17. Electron temperature as a function of the discharge voltage measured with the three probes in the plume near-field. The temperature is computed from the EEDF. (a) Xenon. (b) Krypton.

V. Electron parameters in the plume near-field

A. Electron density

Figures 16a and 16b show the electron density measured in the plasma plume near-field of the PPS®Dual Hall thruster using the Langmuir probes LP1, LP2 and LP3 for different discharges voltages. The density is here calculated from the EEDF. The density magnitude is almost the same for xenon and krypton, but at 300 V where surprisingly it is larger for krypton. This certainly images a different spatial distribution of the density at the channel outlet between xenon and krypton. For the two gases, n_e decreases with the voltage up to 450 V; It increases again at 500 V. This trend originates in the fact that the input power is 3 kW for the first three U_d and it goes up to 5 kW at 500 V, see Tab. 1 and 2. Put another way, the gas flow rate is increased again at 500 V and the discharge current reaches 10 A as in the case of 300 V.

Finally, Fig. 16a and 16b indicate the electron density increases with the distance x to the thruster exit plane for a given operating point, see Tab. 3. This is especially true for xenon. This is a geometrical effect linked to the divergence of the plasma plume.

B. Electron temperature

Figures 17a and 17b show the electron temperature measured in the plasma plume near-field of the PPS®Dual Hall thruster using the Langmuir probes LP1, LP2 and LP3 for different discharges voltages. Unsurprisingly the temperature increases with the discharge voltage for xenon and krypton as in the far-field plume. This is to be expected, since the potential drop governs the electron temperature. The temperature is larger for krypton as its ionization potential is larger. The axial position of the Langmuir probe as almost no impact on the measured temperature.

C. Adiabatic exponent

Figure 18 shows the $\mathrm{Log}(T_e)$ versus $\mathrm{Log}(n_e)$ plots obtained with the LP1, LP2 and LP3 probes for all operating conditions when the PPS®Dual Hall thruster is fueled with xenon. As can be seen, there is no net tendency compared to what we measured in the plume far-field. No values of the adiabatic exponent γ_e can be obtained from the experimental data. This supports the conclusion that γ_e changes with the operating points.

In Fig. 18, blue asterix correspond to the data measured with probe LP1 in order to isolate probe position impact. As can be noticed, $\mathrm{Log}(T_e)$ decreases with $\mathrm{Log}(n_e)$; assuming a linear relationship, the slope is negative that means γ_e is less than 1, which has no physical meaning.

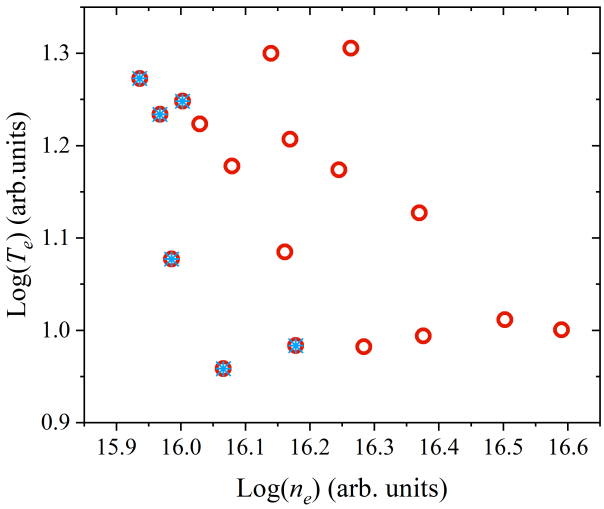

Figure 18. Log(T_e) against Log(n_e) plot in the near-field for xenon in all operating conditions investigated with probes LP1, LP2 and LP3. Light blue asterix are associated with LP1 data.

Figure 19 show the Log(T_e) versus Log(n_e) plots obtained with the LP1, LP2 and LP3 probes for all operating conditions when the PPS®Dual Hall thruster is fueled with krypton. As with xenon there is no net tendency compared to what we measured in the plume far-field. No values of the adiabatic exponent γ_e can be obtained from the experimental krypton data.

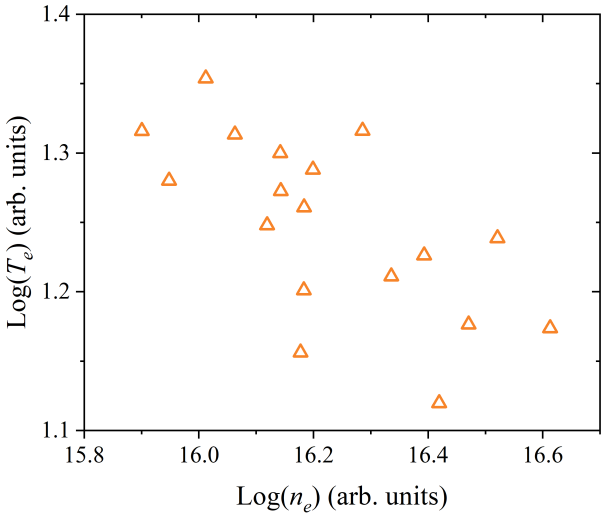

Figure 19. Log(T_e) against Log(n_e) plot in the near-field for krypton in all operating conditions investigated with probes LP1, LP2 and LP3.

D. EEPF

Figure 20 shows the EEPF in the plume near-field computed for OP1 and OP3 with both xenon and krypton as propellant. The EEPF is given for measurements performed with the LP1 probe, i.e. the Langmuir probe the closest to the channel exit plan. A fit to the experimental data with a Maxwellian distribution and a Druyvesteyn distribution is also displayed in Fig. 20. In all cases the distribution function exhibits a

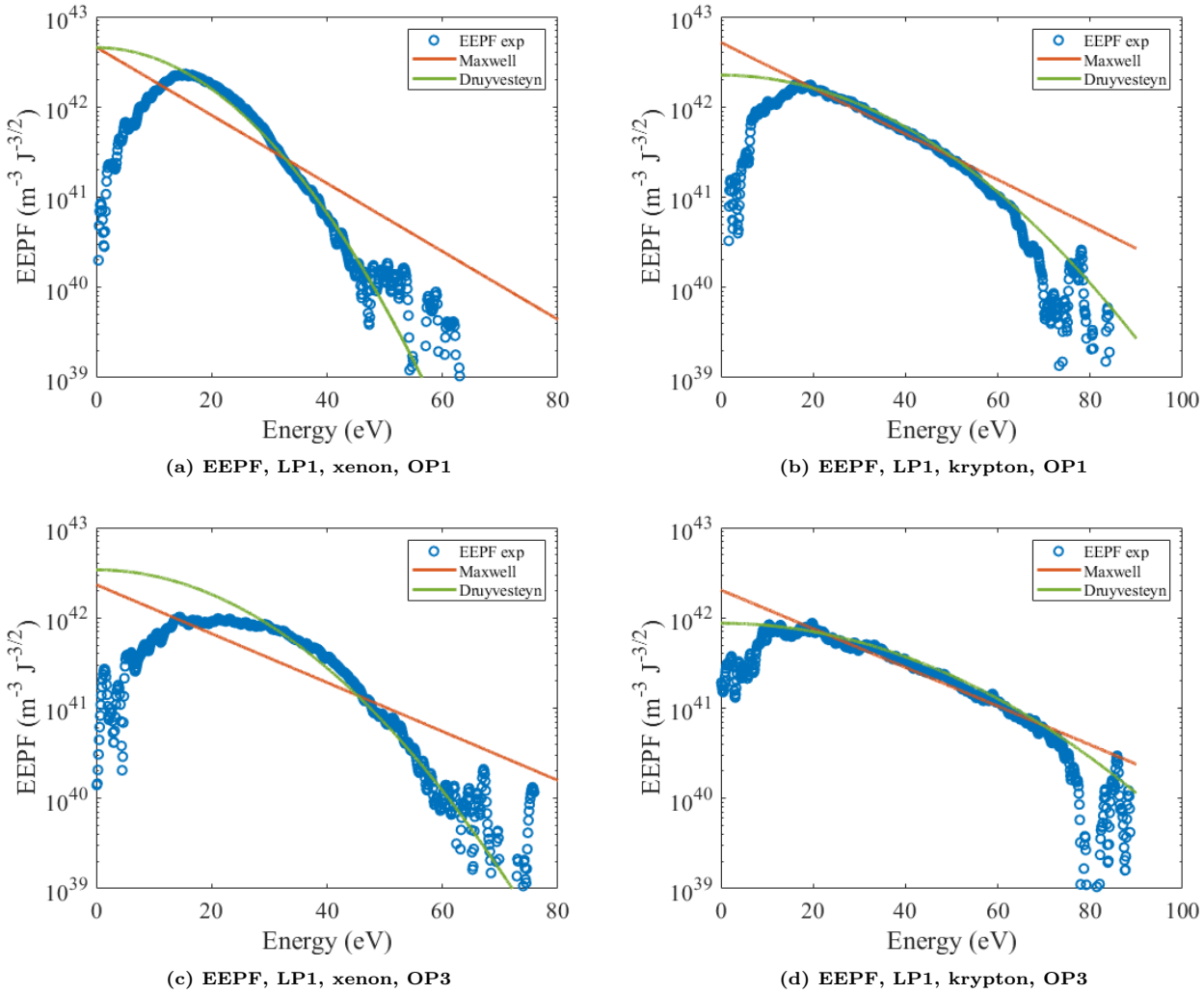

(a) EEPF, LP1, xenon, OP1

(b) EEPF, LP1, krypton, OP1

(c) EEPF, LP1, xenon, OP3

(d) EEPF, LP1, krypton, OP3

Figure 20. EEPF determined with LP1 in the plume near-field for OP1 and OP3 with xenon and krypton. Also shown is a fit with a Maxwellian distribution (red line) and a Druyvesteyn distribution (green line).

large temperature. Data is better described by a Druyvesteyn distribution even though an important dip is observed at very low electron energies. With xenon, we cannot even approximate the data with a Maxwellian distribution of reasonable temperature; The temperature found is much lower than that given by the first-order moment or the slope of the curve Ln(I_e)-V_s.

VI. Conclusion

Time resolved Langmuir probe measurements have been performed in the plasma plume near-field and far-field of the 5 kW-class PPS®Dual Hall thruster in order to extract electron parameters, namely the electron density and the electron temperature. The Hall thruster has been fired with xenon and krypton as propellant for applied voltages from 300 V to 500 V and input power from 3 kW up to 6 kW.

Several conclusions can be drawn from this experimental work. For the two gases, the electron energy distribution function departs from an equilibrium Maxwellian distribution in the near-field and in the far-field. The measured EEDF can be well aprroximated by a Druyvesteyn distribution. Combining electron density and electron temperature data allows the determination of the electron adiabatic exponent γ_e. The latter is below 5/3 for xenon and krypton whatever the operating points. The exponent is lower for xenon and it depends on the thruster conditions. Surprisingly, in the plume far-field γ_e does not depend on the

angular position for a given set of conditions despite large density and temperature gradients between the core of the plume and the edges. In the plume near-field, no value of γ_e could be extracted even for a single probe (fixed position). This supports the idea of a relationship between the adiabatic exponent and the operating parameters.

Futures works can be divided into two parts. Firstly, identical experiments could be carried out with argon as propellant and even with molecular gases like iodine. Secondly, the examination of the electron dynamics would complement this work and provide additional information on the properties of the discharge and the plume. This task could be achieved by performning time-resolved Langmuir probe measurements over a broad range of frequencies.

Acknowledgments

This work has been performed in the frame of the Consortium for Hall Effect Orbital Propulsion System Medium Power program. The CHEOPS Medium Power project has received funding from the European Union's Horizon 2020 research and innovation programme under grant agreement No 101004226.

References

[1]B. Lipschultz, I. Hutchinson, B. LaBombard, and A. Wan. Electric probes in plasmas. *J. Vac. Sci. Technol. A*, 4:1810–1816, 1986.

[2]I. H. Hutchinson. *Principles of Plasma Diagnostics*. Cambridge University Press, New York, 1987.

[3]J. E. Allen. Probe Theory -The Orbital Motion Approach. *Physica Scripta*, 45:497–503, 1992.

[4]V. I. Demidov, S. V. Ratynskaia, and K. Rypdal. Electric probes for plasmas: The link between theory and instrument. *Rev. Sci. Instrum.*, 73:3409–3439, 2002.

[5]F. F. Chen. Lecture notes on Langmuir probe diagnostics. Mini-course on plasma diagnostics, IEEE-ICOPS meeting, Jeju, Korea, 2003.

[6]R. L. Merlino. Understanding Langmuir probe current-voltage characteristics. *Am. J. Phys.*, 75:1078–1085, 2007.

[7]K. Dannenmayer, P. Kudrna, M. Tichý, and S. Mazouffre. Measurement of plasma parameters in the far-field plume of a Hall effect thruster. *Plasma Sources Sci. Technol.*, 20:065012, 2011.

[8]M. Tichý. Plasma diagnostic by probes. Lecture notes for the Tomsk University, Russia, 2015.

[9]K.-U. Riemann. The Bohm criterion and sheath formation. *J. Phys. D : Appl. Phys.*, 24:492–518, 1991.

[10]R. N. Franklin. The plasma–sheath boundary region. *J. Phys. D : Appl. Phys.*, 36:R309–320, 2003.

[11]M. S. Belinov. The Child–Langmuir law and analytical theory of collisionless to collision-dominated sheaths. *Plasma Sources Sci. Technol.*, 18:014005, 2009.

[12]K.-U. Riemann. Plasma and sheath. *Plasma Sources Sci. Technol.*, 18:014006, 2009.

[13]M. S. Belinov. Space-charge sheath with ions accelerated into the plasma. *J. Phys. D: Appl. Phys.*, 43:175203, 2010.

[14]P. Chabert. What is the size of a floting sheath? *Plasma Sources Sci. Technol.*, 23:065042, 2014.

[15]COMSOL Inc. A. Pahl. Electron energy distribution function. `https://www.comsol.com/blogs/electron-energy-distribution-function`, 2014.

[16]T. K. Popov, P. Ivanova, J. Stöckel, and R. Dejarnac. Electron energy distribution function, plasma potential and electron density measured by Langmuir probe in tokamak edge plasma. *Plasma Physics and Controlled Fusion*, 51:065014, 2009.

[17]V. A. Godyak and R. B. Piejak B. M. Alexandrovich. Electron energy distribution function measurements and plasma parameters in inductively coupled argon plasma. *Plasma Sources Sci. Technol.*, 11:525–543, 2002.

[18]K. Takahashi, C. Charles, R. W. Boswell, and T. Fujiwara. Electron Energy Distribution of a Current-Free Double Layer: Druyvesteyn Theory and Experiments. *Phys. Rev. Lett.*, 107:035002, 2011.

[19]M. Tichý, A. Pétin, P. Kudrna, M. Horkỳ, and S. Mazouffre. Electron energy distribution function in a low-power Hall thruster discharge and near-field plume. *Phys. Plasmas*, 25:061205, 2018.

[20]G. Giono, J. T. Gudmundsson, N. Ivchenko, S. Mazouffre, K. Dannenmayer, D. Loubére, L. Popelier, M. Merino, and G. Olentšenko. Electron energy distribution function in a low-power Hall thruster discharge and near-field plume. *Plasma Sources Sci. Technol.*, 27:015006, 2018.

[21]A. Caldarelli, F. Filleul, R. W. Boswell, C. Charles, N.J. Rattenbury, and J.E. Cater. Data Processing Techniques for Ion and Electron Energy Distribution Functions. *Phys. Plasmas*, 30:040501, 2023.

[22]H. Amemiya. Sheath formation criterion and ion flux for non-Maxwellian plasma. *J. Physical Society Japan*, 66:1335–1338, 1997.

[23]V. A. Godyak and R. B. Piejak B. M. Alexandrovich. Measurement of electron energy distribution in low-pressure RF discharges. *Plasma Sources Sci. Technol.*, 1:36–58, 1992.

[24]H. Mott-Smith and I. Langmuir. The theory of collector in gaseous discharges. *Phys. Rev.*, 28:727–763, 1926.

[25]I. D. Sudit and R. C. Woods. A study of the accuracy of various Langmuir probe theories. *J. Appl. Phys.*, 76:4488–4498, 1994.

[26]F. F. Chen. Langmuir probes in RF plasma: surprising validity of OML theory. *Plasma Sources Sci. Technol.*, 18:035012, 2009.

[27]F. F. Chen. *Introduction to plasma physics and controlled fusion*. Plenum Press, New York, 1984.

[28]M. A. Lieberman and A. J. Lichtenberg. *Principles of Plasma Discharges and Materials Processing*. John Wiley & Sons, Inc., New York, 1994.

[29]T. E. Sheridan. How big is a small Langmuir probe? *Phys. Plasmas*, 7:3084, 2000.

[30]R. J. Umstattd, C. G. Carr, C. L. Frenzen, J. W. Luginsland, and Y. Y. Lau. A simple physical derivation of the Child-Langmuir space-charge-limited emission using vacuum capacitance. *Am. J. Phys.*, 73:160–163, 2005.

[31]S. Mazouffre. Ion current density measurement in the plume of Hall thrusters: Theory and instruments. Scientific report PE-R-01-2016, CNRS, ICARE, Orléans, France, in French, 2016.

[32]R. R. Puri, B. Debabrata, and R. Kumar. Generalization of the Child-Langmuir law for nonzero injection velocities in a planar diode. *Physics of Plasmas*, 11:1178–1186, 2004.

[33]K. Burm and W. J. Goedheerand D. C. Schram. The isentropic exponent in plasmas. *Phys. Plasmas*, 6:2622–2627, 1999.

[34]K. Dannenmayer and S. Mazouffre. Electron flow properties in the far-field plume of a Hall thruster. *Plasma Sources Sci. Technol.*, 22:035004, 2013.

[35]J. M. Little and E. Y. Choueiri. Electron Cooling in a Magnetically Expanding Plasma. *Phys. Rev. Lett.*, 117:225003, 2016.

[36]Y. Zhang, C. Charles, and R.Boswell. Thermodynamic Study on Plasma Expansion along a Divergent Magnetic Field. *Phys. Rev. Lett.*, 116:025001, 2016.

[37]K. Takahashi, C. Charles, R.Boswell, and A. Ando. Adiabatic Expansion of Electron Gas in a Magnetic Nozzle. *Phys. Rev. Lett.*, 120:045001, 2018.

[38]K. Takahashi, C. Charles, R.Boswell, and A. Ando. Thermodynamic Analogy for Electrons Interacting with Magnetic Nozzle. *Phys. Rev. Lett.*, 125:165001, 2020.

[39]J. Y. Kim, G.Go, Y. S. Hwang, and K. J. Chung. Dependence of the polytropic index of plasma on magnetic field. *New J. Phys.*, 23:052001, 2021.

[40]A. E. Vinci, Q. Delaviè–Delion, and S. Mazouffre. Electron thermodynamics along magnetic nozzle lines in a helicon plasma. *J. Electric Propulsion*, 1:1–12, 2022.

[41]J. M. Rax. *Physique des Plasmas*. Dunod, Paris, 2005.

[42]P. Chabert and N. Braithwaite. *Physics of Radio-Frequency Plasmas*. Cambridge University Press, Cambridge, 2011.

[43]R. A. Serway and Jr. J. W. Jewett. *Physics for Scientists and Engineers with Modern Physics*. Wadsworth Publishing Co Inc; 9th ed., Boston, 2013.

[44]M. Li, S. Dew, and M. J. Brett. Effect of electron distribution functions on the floating potential of particles in the plasma: thin plasma sheaths. *J. Phys. D: Appl. Phys*, 32:2056–2059, 1999.

A. Electron energy distribution function

The electron energy distribution function (EEDF) refers to the probability density function that describes the energy distribution of electrons within a plasma. It provides valuable information about the population of electrons at various energies and velocities. To describe the EEDF, several possibilities are available, such as a Maxwell or a Druyvesteyn function. These two specific distribution functions assume that elastic collisions dominate, thus the effect of inelastic collisions (e.g., excitation or ionization) on the distribution function is neglected or insignificant. In such a case, the distribution function becomes spherically symmetric.

A. Maxwellian EEDF

In a system containing a large number of non-relativistic electrons in thermodynamic equilibrium with temperature T_e, the fraction of the particles within an infinitesimal element of the three-dimensional velocity space $d^3v = dv_x dv_y dv_z$, centered on a velocity vector $\mathbf{v}$ of magnitude v reads:

$$f(\mathbf{v}) = n_e \left(\frac{m_e}{2\pi k_B T_e}\right)^{3/2} \exp\left(-\frac{m_e v^2}{2k_B T_e}\right). \tag{17}$$

The function $f(\mathbf{v})$ is the stationary ($\partial f/\partial v = 0$) Maxwellian velocity (vector) distribution function.[27,41–44] It is a probability distribution function, normalized so that:

$$\int f(\mathbf{v}) d^3v = n_e. \tag{18}$$

For an isotropic distribution, one can write the element of velocity space as $d^3v = 4\pi v^2 dv$ after integrating over a sphere. The velocity distribution is then given by:

$$f(\mathbf{v}) d^3v = n_e 4\pi v^2 \left(\frac{m_e}{2\pi k_B T_e}\right)^{3/2} \exp\left(-\frac{m_e v^2}{2k_B T_e}\right) dv = f(v)dv, \tag{19}$$

where $f(v)$ is the probability distribution of speeds (velocity magnitude $v^2 = v_x^2 + v_y^2 + v_z^2$). The function $f(v)$ can be instead writen in terms of kinetic energy ε:

$$\varepsilon = \frac{1}{2} m_e v^2 = eV, \tag{20}$$

where V is the potential. For a Langmuir probe, $V = V_p - V_s$. Combining Eq. 19 and Eq. 20 gives:

$$\begin{aligned} f(v)dv &= n_e 4\pi v^2 \left(\frac{m_e}{2\pi k_B T_e}\right)^{3/2} \exp\left(-\frac{m_e v^2}{2k_B T_e}\right) dv & (21)\\ &= \frac{2n_e}{\sqrt{\pi}} \left(\frac{1}{k_B T_e}\right)^{3/2} \varepsilon^{1/2} \exp\left(-\frac{\varepsilon}{k_B T_e}\right) d\varepsilon, & (22)\\ &= g(\varepsilon)d\varepsilon. & (23) \end{aligned}$$

The function $g(\varepsilon)$ is the Maxwellian electron energy distribution function (EEDF) expressed in $\mathrm{m^{-3}\,J^{-1}}$:

$$g_M(\varepsilon) = \frac{2n_e}{\sqrt{\pi}} \left(\frac{1}{k_B T_e}\right)^{3/2} \varepsilon^{1/2} \exp\left(-\frac{\varepsilon}{k_B T_e}\right). \tag{24}$$

The expression $\hat{g(\varepsilon)} = g(\varepsilon)/\sqrt{\varepsilon}$ is the electron energy probability function (EEPF) expressed in $\mathrm{m^{-3}\,J^{-3/2}}$. The $\hat{g(\varepsilon)}$ function gives a straight line on a semilog plot, hence its usefulness.

B. Druyvesteyn EEDF

The Maxwellian EEDF relies on a constant elastic collision frequency, inelastic collisions being neglected. On-the contrary the Druyvesteyn EEDF assumes a constant, electron-energy-independent cross section.[15,18,20,22,41,44] This leads to a drop of the EEDF at high electron energies for the same mean electron energy.

A generalized EEDF g_G can be expressed as:

$$g_G(\varepsilon) = \frac{n_e}{(k_B T_e)^{3/2}} \beta_1 \sqrt{\varepsilon} \exp\left[-\beta_2 \left(\frac{\varepsilon}{k_B T_e}\right)^x\right], \tag{25}$$

where x is a parameter giving the shape of the EEDF and β_1 and β_2 are constants that depends upon x:

$$\beta_1 = 2\left(\frac{2}{3}\right)^{3/2} \Gamma(\xi_1)^{-5/2} \Gamma(\xi_2)^{3/2} \qquad \text{and} \qquad \beta_2 = \left(\frac{2}{3}\right)^x \left(\frac{\Gamma(\xi_2)}{\Gamma(\xi_1)}\right)^x, \tag{26}$$

with

$$\xi_1 = \frac{3}{2x} \qquad \text{and} \qquad \xi_2 = \frac{5}{2x}. \tag{27}$$

$\Gamma(\xi)$ is the complete Gamma function defined as:

$$\Gamma(\xi) = \int_0^\infty t^{\xi-1} \exp(-t) dt. \tag{28}$$

The case $x = 1$ corresponds to a Mawxellian EEDF:

$$\beta_1 = 1.128 = \frac{2}{\sqrt{\pi}}, \tag{29}$$

$$\beta_2 = 1. \tag{30}$$

The case $x = 2$ corresponds to a Druyvesteyn EEDF:

$$\beta_1 = 0.5652 \quad (= \frac{4\Gamma(1/4)^4}{\pi(12\sqrt{2}\pi)^{3/2}} \quad \text{after Li et al}), \tag{31}$$

$$\beta_2 = 0.243. \tag{32}$$

The Druyvesteyn energy distribution therefore reads:

$$g_D = 0.5648 \frac{n_e}{(k_B T_e)^{3/2}} \sqrt{\varepsilon} \exp\left[-0.243 \left(\frac{\varepsilon}{k_B T_e}\right)^2\right]. \tag{33}$$